Advanced Functional Materials

ADVANCED FUNCTIONAL MATERIALS
www.afm-journal.de

RESEARCH ARTICLE

Dual Confinement Modulation in Perovskite Nanocrystals Enabled Near-Standard-Green Emission With Invariant Chromaticity

Eojin Yoon[1] | Kyoo-Hyung Lee[1] | Chan-Yul Park[1] | Min-Jun Sung[1] | Yuxin Shi[1] | Kyung Yeon Jang[1] | Jinwoo Park[1] | Joo Sung Kim[1] | Eonsu Kim[1] | Tae-Woo Lee[1,2,3,4]

[1]Department of Materials Science and Engineering, Seoul National University, Seoul, Republic of Korea | [2]Institute of Engineering Research, Soft Foundry, Research Institute of Advanced Materials, Seoul National University, Seoul, Republic of Korea | [3]Interdisciplinary Program in Bioengineering, Seoul National University, Seoul, Republic of Korea | [4]SN DISPLAY Co. Ltd., Seoul, Republic of Korea

Correspondence: Tae-Woo Lee (twlees@snu.ac.kr)

Received: 3 December 2025 | **Revised:** 16 February 2026 | **Accepted:** 3 March 2026

Keywords: dielectric confinement | near-standard-green emission | perovskite nanocrystal | quantum confinement | surface reconstruction

ABSTRACT

Quantum and dielectric confinement critically govern the intrinsic emission wavelength of perovskite nanocrystals, however achieving precise and simultaneous control over both remains challenging. Here, we report a surface-driven reconstruction strategy for in situ-formed nanocrystals on the substrate, enabling dual confinement modulation. In this process, the originally attached bulky organic ammonium ligands reorganize to promote crystal growth, whereas the subsequently introduced covalently bound phosphonic acid ligands control particle size and co-assemble into a compact dielectric shell. Spectroscopic ellipsometry reveals an increased dielectric permittivity of the ligand shell, indicating enhanced dielectric screening that modulates Coulomb interactions and induces band-edge renormalization, enabling finely tunable redshifts into the near-standard green emission regime. The emission followed an empirical bandgap relation governed by nanocrystal size and the local dielectric environment, revealing that surface-driven reconstruction of substrate-grown in situ nanocrystals provides deterministic control over both quantum and dielectric confinement. Devices exhibited near-standard-green emission at (0.177, 0.769) with exceptionally small chromaticity deviation of $\Delta u'v' \leq 0.0014$ across the operating voltage range and ≤ 0.0027 from over a viewing range of 0°–80°, far outperforming the tolerances required for advanced display (≤ 0.02), medical imaging systems (≤ 0.01) and AR/VR devices of 0.007.

1 | Introduction

Metal halide perovskites have emerged as highly attractive light-emitting materials owing to their facile spectral tunability, intrinsically narrow emission linewidths, versatile processability and cost-effective precursors. Over the past decade, the development of perovskite light-emitting diodes (PeLEDs) has advanced remarkably, achieving substantial improvements in both efficiency and operational stability [1–7]. However, despite significant advances, most state-of-the-art PeLEDs still suffer from chromaticity deviation, as their emission peaks are displaced from the pure-green region in the CIE color space [5–7]. Therefore, there is a growing demand for perovskite emitters to deliver comparable color precision while maintaining their intrinsic advantages in processability and efficiency.

Eojin Yoon and Kyoo-Hyung Lee equally contributed to this work.

To meet the color requirements of modern and future display technologies, emitters must achieve near-standard-green emission that fully covers the DCI-P3 standard while approaching the Rec.2020 in the CIE chromaticity diagram. The DCI-P3 gamut represents the commercialized industry benchmark, whereas Rec.2020 defines the next-generation ultra-wide color space aimed at AR/VR and high-fidelity imaging. Consequently, materials that can bridge these two standards are essential for ensuring both commercial compatibility and future expandability. Because the green coordinates of DCI-P3 (0.265, 0.690) and Rec.2020 (0.170, 0.797) differ considerably, precise wavelength tuning within a few nanometers is required to simultaneously satisfy both color spaces. Moreover, practical emitters must maintain such color precision under realistic operating conditions. In display applications, chromaticity invariance across driving voltages and viewing angles is a critical metric, as spectral shifts cause visible color distortion [8, 9]. Accordingly, the chromaticity deviation of $\Delta u'v'$ must remain below the established tolerances of advanced display ($\leq$0.02), medical imaging systems ($\leq$0.01).

Fine wavelength tuning in metal halide perovskites has been mainly pursued by compositional and synthetic strategies. Halide anion substitution has been a major strategy for bandgap engineering, but mixed-halide systems inevitably suffer from segregation, making them unsuitable for precise and stable wavelength control [10, 11]. Rather, A-site cation alloying provides a refined route by expanding the lattice constant through the incorporation of larger cations, which weakens orbital overlap and induces a moderate redshift. Spectrally pure green PeLEDs have been demonstrated by optimizing the Cs/FA ratio or incorporating dopants to suppress trap states [12], and further improvements have been achieved using FA/Cs/GA alloying combined with multifunctional additives [13]. Beyond compositional approaches, the electronic bandgap in nanocrystals can be regulated through intrinsic confinement effects, with quantum confinement dictated by particle size and dielectric confinement arising from the contrast in permittivity between the core and its surroundings [14]. These effects have been explored using strategies such as dielectric screening achieved by increasing the shell thickness in colloidal quantum dots [15], phase- and morphology-dependent confinement in Cs-Pb-Br nanocrystals [16], and the incorporation of high-permittivity spacer ligands in quasi-2D perovskites to reduce dielectric confinement and lower exciton binding energy [17, 18]. While these approaches demonstrate that confinement effects offer powerful levers for spectral control, they primarily rely on modifying isolated aspects of the nanocrystal, either its size, phase, or dielectric environment, rather than integrating both quantum and dielectric confinement in a unified material design. Consequently, an integrated approach capable of tuning both nanocrystal size and dielectric surroundings to realize fine wavelength control in the near-standard-green range has been less explored.

In this work, we established a composition-invariant intrinsic route to modulate both quantum and dielectric confinement within perovskite nanocrystals through an on-substrate surface reconstruction process. Bulky ammonium ligands were initially incorporated into the precursor solution to induce in situ formation of perovskite nanocrystals on the substrate. During subsequent surface reconstruction, these weakly bound species dynamically rearranged, and the introduction of covalently anchored phosphonic acid ligands reinforced the surface. Through cooperative coordination of the phosphonic acid ligands with the reorganized ammonium moieties, a compact hybrid shell could be formed, and this concurrently suppressed surface traps and enhanced the local dielectric environment. This sequential reconstruction enables fine adjustment of the bandgap through two correlated parameters, the nanocrystal size and the shell permittivity. As a result, the photoluminescence peak could be finely tuned within the 520–530 nm range by controlling the reaction time, along with decrease in exciton confinement. Ellipsometric analysis combined with effective medium modeling verified the dielectric enhancement and revealed a quantitative correlation between dielectric screening and the observed emission shifts, confirming that the spectral tunability originates from coupled confinement modulation. The resulting in situ nanocrystal films preserve excitonic emission characteristics and maintain spectral integrity under electrical excitation and angular variation, underscoring the robustness of this approach. The devices further exhibited color-stable near-standard-green emission at (0.177, 0.769) with extremely small chromaticity deviations ($\Delta u'v' \leq$0.0014 across the operating voltage range and $\leq$0.0027 over a viewing angle range between 0°–80°), fully covering the DCI-P3 gamut and exhibiting proximity to the Rec.2020 color gamut.

2 | Results and Discussion

2.1 | Defining Near-Standard-Green Window and Confinement-Driven Bandgap Modulation

As conceptually illustrated in Figure 1A, perovskite in situ nanocrystals with controlled dual confinement were synthesized by employing substrate-grown nanocrystals in combination with a post synthetic treatment. The substrate grown nanocrystals were prepared by adding a spacer ligand contining bulky ammonium functional groups to the peovskite precursor solution. The ligand was added at 30 to 50 mol% with respect to $PbBr_2$ to regulate crystal nucleation and growth, and the nanocrystal pinning process was treated on spin-coating film, which immobilizes nuclei to control the size distribution [4, 19–21]. The in situ nanocrystal diameter (8.70 nm) is slightly smaller than the exciton Bohr diameter of 10 nm, resulting in pronounced quantum and dielectric confinement due to the substantial permittivity contrast at the core-shell interface [22]. To alleviate these confinement effects for near-standard-green emission, we introduced a post-synthetic treatment to the substrate-grown nanocrystals. The increased size of nanocrystals relaxed the quantum confinement and also the compact dielectric ligand shell with additional phosphonic acids decreased the permittivity mismatch between the core and the shell. Moreover, phosphonic acids effectively passivated uncoordinated Pb sites, providing additional suppression of trap states.

Near-standard green emission refers to the spectral region that covers both the DCI-P3 commercial standard and the Rec.2020 next generation standard in the chromaticity diagram. As shown in Figure 1B and Figure S1, the CIE coordinates were obtained by sweeping the peak emission wavelength of our reference perovskite film with full-width half maximum (FWHM) of 22.17 nm

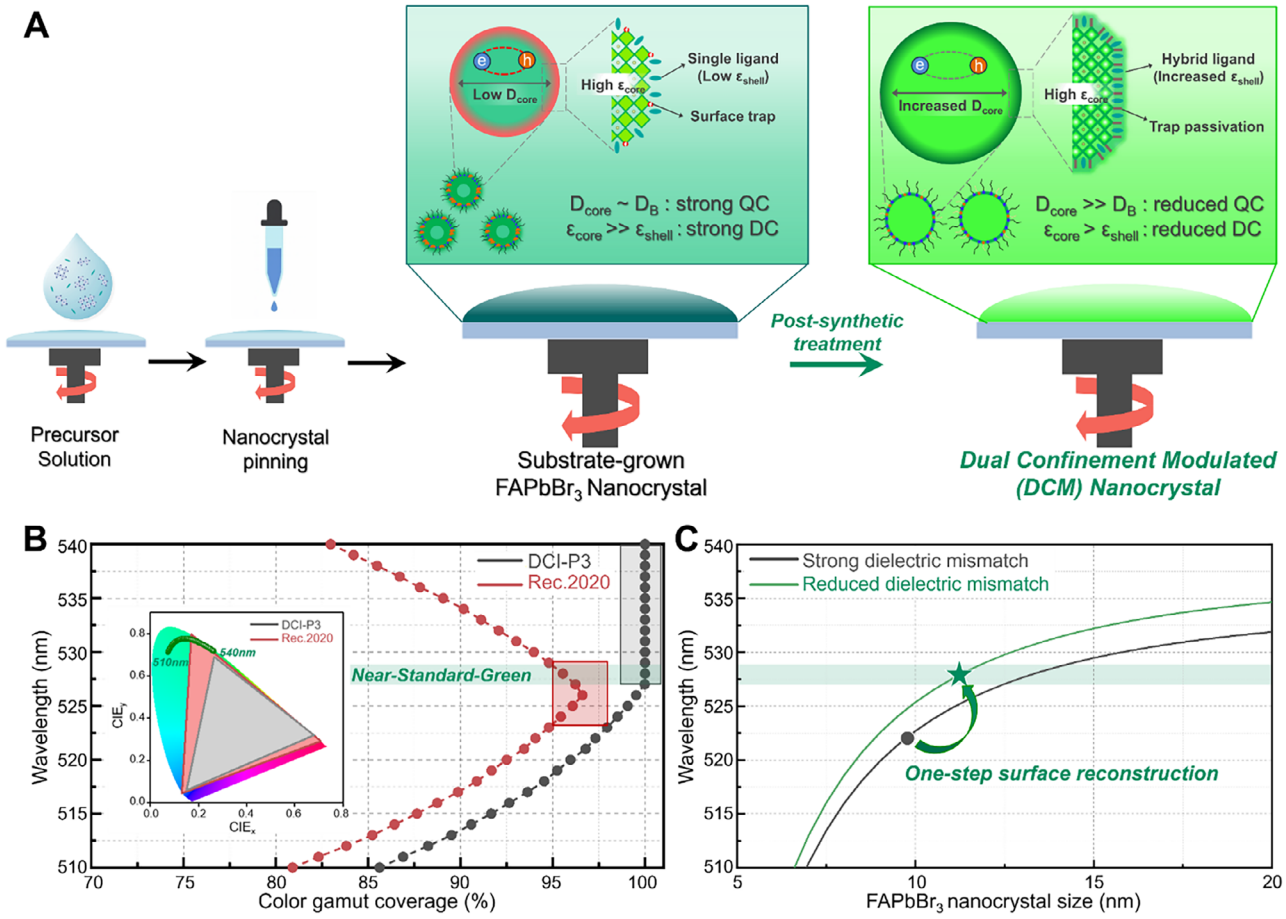

FIGURE 1 | Dual confinement modulation of perovskite nanocrystals for spectral control in the near-standard-green emission window. (A) Schematic illustration of nanocrystal surface reconstruction and dual confinement modulation. (B) Definition of the near-standard-green emission window based on spectral coverage of DCI-P3 and Rec.2020 color standards. (C) Schematic representation of emission wavelength tuning via combined quantum and dielectric confinement effects.

from 510 to 540 nm and calculated the corresponding gamut coverage using its measured spectrum as the fixed lineshape. DCI-P3 reached complete coverage when the peak wavelength exceeded 527 nm and Rec.2020 achieved highest coverage of 96.22% at 527 nm, followed by a steep decline as wavelength shifts. We considered the near-standard-green window as the spectral range that provides complete coverage of DCI-P3 while simultaneously including more than 95% coverage of Rec.2020. The overlap of the two standards was limited to a narrow range from 527 to 529 nm. Such a narrow window demonstrates the critical need for precise spectral tuning in perovskite emitters. Figure 1C illustrates the impact of quantum and dielectric confinement on the emission wavelength of $FAPbBr_3$ in situ nanocrystals, which is influenced by the nanocrystal size and the dielectric constant of the surrounding shell, and the bandgap of perovskite nanocrystals can be expressed as the bulk bandgap with additional contributions from these confinement effects [22]. While single crystal $FAPbBr_3$ exhibits a bandgap of about 2.15 eV, the emission spectrum of nanocrystals significantly blueshifts owing to the strong quantum confinement effect [23]. Based on these correlations, we modulated both quantum and dielectric confinements to effectively tune the emission wavelength, achieving near-standard-green emission.

2.2 | Unraveling Nanocrystal Reconstruction Mechanism

The reference in situ $FAPbBr_3$ nanocrystals were synthesized using the bulky ammonium ligand phenylethylammonium (PEA) at 35 mol% relative to Pb, while a small amount of crown ether was added to the precursor solution to act as a dispersing agent and suppress PEA aggregation, thereby promoting uniform nanocrystal formation. In addition, the introduction of a very thin 4 nm LiF interlayer further facilitated uniform crystallization. We investigated the impact of the post-synthetic treatment on the crystal structure and surface chemistry of perovskite in situ nanocrystals. To decouple the roles of the solvent THF alone and the covalently binding phosphonic ligand introduced in the THF-based treatment, two types of post-treated nanocrystal samples were prepared. For clarity, nanocrystals terminated only with bulky ammonium ligands were denoted as ammonium terminated nanocrystals (AT-NC), which served as the reference sample. Samples treated only with THF were referred to as rearranged nanocrystals (RA-NC), whereas those treated with both THF and the phosphonic acid ligand were designated as hybrid-terminated nanocrystals (HT-NC). Figure 2A–D presents grazing-incidence wide-angle x-ray scattering (GIWAXS) patterns

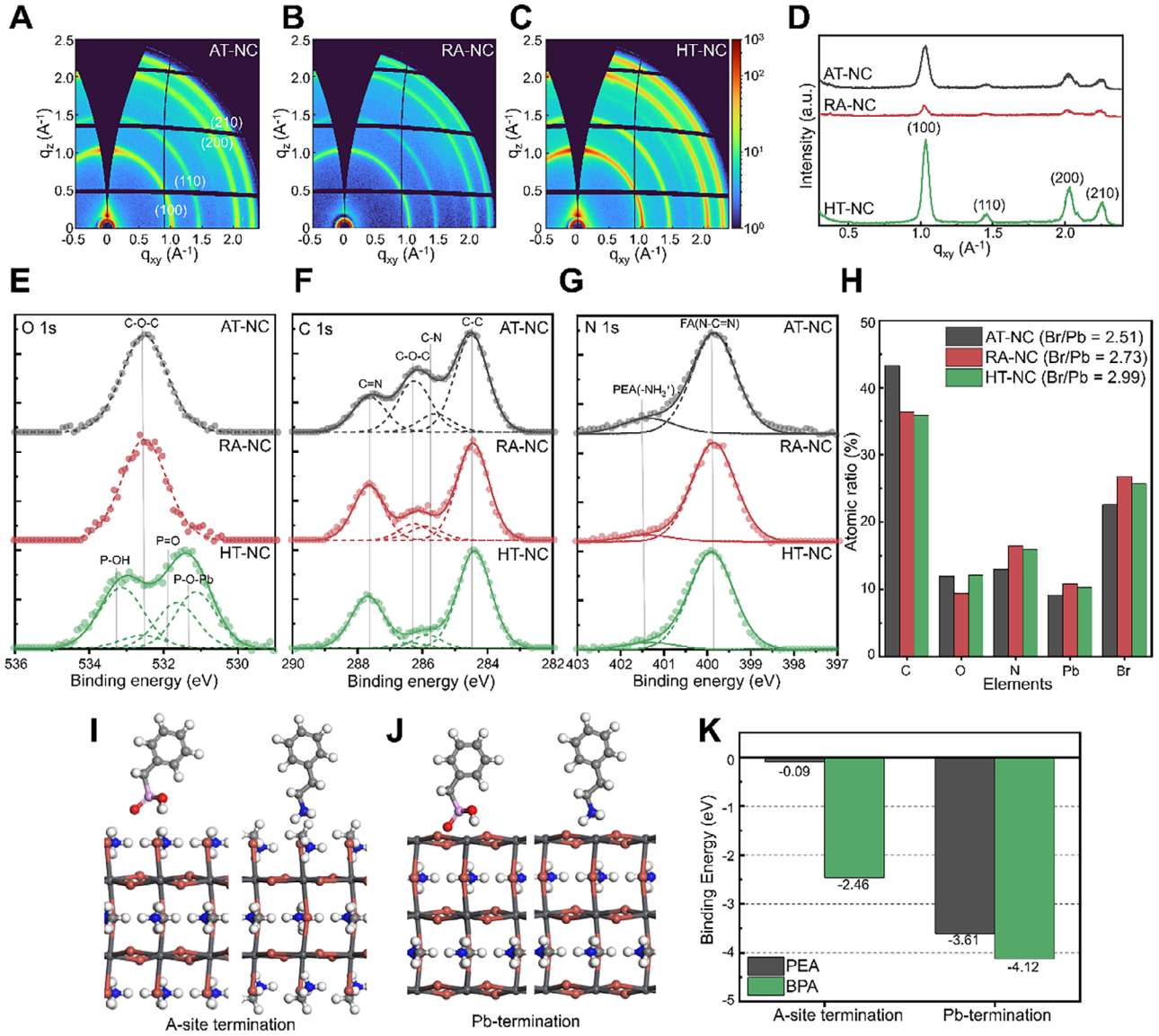

FIGURE 2 | Structural and surface reorganization of perovskite nanocrystals under different post-synthetic treatments. (A–C) GIWAXS patterns of AT-NC, RA-NC, and HT-NC films. (D) Corresponding integrated 1D GIWAXS profiles ($q_z = 0$). (E–G) High-resolution XPS spectra of (E) O 1s, (F) C 1s, and (G) N 1s, revealing the chemical environments of the surface ligands and perovskite components. (H) Elemental atomic ratios and the corresponding Br/Pb ratios of the films. (I–K) DFT calculation results: Schematic illustrations of ligand adsorption states on (I) A-site terminated and (J) Pb-terminated perovskite surfaces. (K) Calculated binding energies of PEA and BPA ligands as a function of the surface termination.

of in situ nanocrystal films prepared under different conditions. All samples exhibited diffraction peaks corresponding to the 3D $FAPbBr_3$ phase at the (100), (110), (200), and (210) planes, with no evidence of additional phase formation [24]. This indicates that the post-treatment processes do not induce phase transitions, and the reactions predominantly occur at the nanocrystal surface. Notably, the in-plane reciprocal space maps at $q_z = 0$ reveal clear differences in peak intensity among the samples. Among the three samples, the RA-NCs exhibited the weakest diffraction signals, the AT-NCs showed moderate intensity, and the HT-NCs displayed the strongest peaks. The concurrent increase in every phase reflection with narrower peak widths indicates that the HT-NCs possess enhanced structural order with reduced lattice disorder [25]. Crystallite sizes estimated from the (100) peak of $FAPbBr_3$ using the Scherrer equation were 8.70 nm for the AT-NCs, 12.29 nm for the RA-NCs, and 10.88 nm for the HT-NCs.

To further examine the structural evolution of the nanocrystals, transmission electron microscopy (TEM) analysis was performed (Figure S2). The TEM images show well-dispersed nanocrystals for all samples, and statistical analysis yields average particle sizes of 9.15 ± 1.89 nm for AT-NCs, 12.50 ± 3.06 nm for RA-NCs, and 11.52 ± 2.83 nm for HT-NCs (Figure S2D). The TEM-based particle sizes are slightly larger than the crystallite sizes estimated from GIWAXS, which can be attributed to the presence of multi-domain nanocrystals observed in HRTEM (Figure S2E,F). Lattice fringes with a spacing of 0.297 nm are consistent with the (200) plane of pseudocubic $FAPbBr_3$ [3].

To elucidate the surface-driven nanocrystal reconstruction mechanism from the perspective of the chemical binding environment, we performed a comprehensive x-ray photoelectron spectroscopy (XPS) analysis (Figure 2E–H; Figure S3). The O 1s spectra

(Figure 2E) of the AT-NC and RA-NC films exhibit intense peaks corresponding to the C—O—C ether linkages, originating from the crown ether ligands. In contrast, the HT-NC films show a marked suppression of this signal, indicating a substantial displacement of crown ethers upon the introduction of phosphonic acid. This observation is further corroborated by the C 1s spectra (Figure 2F), where a significant intensity reduction is observed in the 285–287 eV range. This region, which can be deconvoluted into C—O—C (~ 286.3 eV) and C-N (~ 285.8 eV) components associated with crown ether and PEABr, respectively, reveals a more pronounced attenuation in HT-NC compared to RA-NC. Such a trend suggests that the BPA molecules effectively outcompete the crown ethers for surface Pb^{2+} sites. Unlike the crown ethers, which rely on relatively labile dative coordination through oxygen lone pairs, the phosphonate groups in BPA establish thermodynamically stable P—O—Pb linkages with a more pronounced covalent character (Figure 2E) [5]. This systematic ligand evolution is also reflected in the N 1s spectra (Figure 2G), which were deconvoluted into the N—C=N resonance of the FA cation and the $-NH_3^+$ group of the PEA ligand. In both RA-NC and HT-NC, the $-NH_3^+$ peak intensity decreases, confirming that the THF-driven rearrangement process is inherently accompanied by partial ligand removal. Notably, time-resolved XPS analysis (Figures S4–S6) reveals significant spectral shifts even at remarkably short reaction intervals of 2, 6, and 10 s. This demonstrates that the ligand exchange and surface reconstruction occur almost instantaneously upon solvent exposure, effectively addressing the kinetic feasibility of such rapid morphological evolution. Such second-scale surface reconstruction is consistent with prior reports that ligand binding in lead halide perovskite nanocrystals is highly dynamic, where weakly bound ligands can undergo rapid exchange and desorption upon exposure to polar solvents [26]. In addition, the subsequent structural evolution can proceed through local nanocrystal coalescence driven by surface-energy minimization, without requiring long-range mass transport or classical Ostwald ripening [27]. The displacement of crown ether and PEA is further confirmed by FT-IR (Figure S7), showing marked attenuation of $\nu(C-O-C)$ (~1100 cm^{-1}), $\nu(skeletal)$ (~960 cm^{-1}), and $\rho(-NH_3^+)$ (~ 835 cm^{-1}) vibrations.

Importantly, the solvation-induced ligand detachment is a key driver for the observed morphological evolution. The detachment of PEABr and crown ether, which previously acted as steric barriers between individual nanocrystals, facilitates grain coalescence and structural reorientation (Figure S8). This process allows for the fusion of smaller nanocrystals into larger and higher-crystallinity domains. In HT-NC, the introduced BPA molecules act as strong anchors during this growth phase, ensuring a controlled reconstruction that effectively passivates surface defects and stabilizes the perovskites (Figure S8). In contrast, the RA-NC films undergo uncontrolled ligand detachment, which disrupts surface charge compensation and generates undercoordinated Pb^{2+} sites. These Pb-rich surface environments can facilitate electron accumulation and partial reduction of Pb^{2+} to metallic Pb^0 (Figure S3) [28]. This chemical transformation is quantitatively supported by the increase of the Br/Pb atomic ratio (Figure 2H). While the initial AT-NC film exhibits a Br-deficient stoichiometry (Br/Pb = 2.51), suggesting a high density of halide vacancies, the ratio increases to almost ideal value of 2.99 for HT-NC. This stoichiometric restoration in HT-NC indicates that BPA molecules effectively suppress the loss of halide anions during the solvation-induced detachment and facilitate the formation of a defect suppressed perovskite lattice. Furthermore, top-view SEM analysis confirmed that all three films maintain a highly uniform, pinhole-free morphology (Figure S9). This indicates that the observed surface reconstruction and defect formation occur primarily at the microscopic level without inducing macroscopic film defects.

To theoretically substantiate these surface interactions, density functional theory (DFT) calculations were conducted on a perovskite slab model (Figure 2I–K). The results demonstrate that BPA possesses consistently superior binding affinities compared to PEA across diverse surface terminations, providing a universal thermodynamic drive for the observed ligand exchange process. While the anchoring is particularly robust at the Pb-termination (−4.12 eV), the enhanced binding energy of BPA on surface site ensures a more stable chemical environment than its PEA counterpart. Conversely, the negligible binding energy of PEA at the A-site (−0.09 eV) underscores its labile nature, enabling it to function as a dynamic growth template that facilitates nanocrystal coalescence during the initial reconstruction phase.

2.3 | Confinement-Driven Optical Properties

Subsequently, we analyzed the effect of surface reconstruction on the optical properties of the in situ perovskite nanocrystal films. Steady-state photoluminescence (PL) and UV–vis measurements were first carried out to probe the emission wavelength and intensity (Figure 3A). The AT-NC films exhibited an emission peak at 520 nm, which can be attributed to strong quantum confinement in the small crystallites. In contrast, the RA-NC and HT-NC films showed redshifted emission centered at 529 nm, accompanied by corresponding redshifted absorption edges. The RA-NCs exhibited a decrease in PL intensity due to dominant nonradiative recombination arising from defects exposed by ligand detachment during the reconstruction process. In contrast, the HT-NCs showed a steep increase in PL intensity because cationic surface defects were additionally passivated by the introduced phosphonic acid. Notably, despite the larger crystallite size of the RA-NCs compared to the HT-NCs, the two films exhibited nearly identical PL peak positions. This observation indicates that the emission energy does not scale monotonically with crystallite size and cannot be explained solely by quantum confinement effects.

To further examine confinement-related effects, temperature-dependent steady-state PL (TDPL) measurements were performed from 130 to 300 K (Figure 3B,C). The temperature dependence of PL intensity was fitted using the Arrhenius equation to extract the thermal activation energy (E_a). Under the assumption that nonradiative recombination is primarily governed by exciton dissociation rather than trap-assisted pathways, the extracted E_a reflects the relative strength of exciton binding in the nanocrystal films [29]. The AT-NC film exhibited the highest E_a of 156.18 meV, whereas the RA-NC and HT-NC films showed comparable and significantly lower E_a values of 103.19 meV and 105.45 meV, respectively. Despite their different crystallite sizes, the nearly identical E_a values of the RA-NC and HT-NC films suggest that the decreased quantum confinement alone due to the increase crystallite size is insufficient to account for the

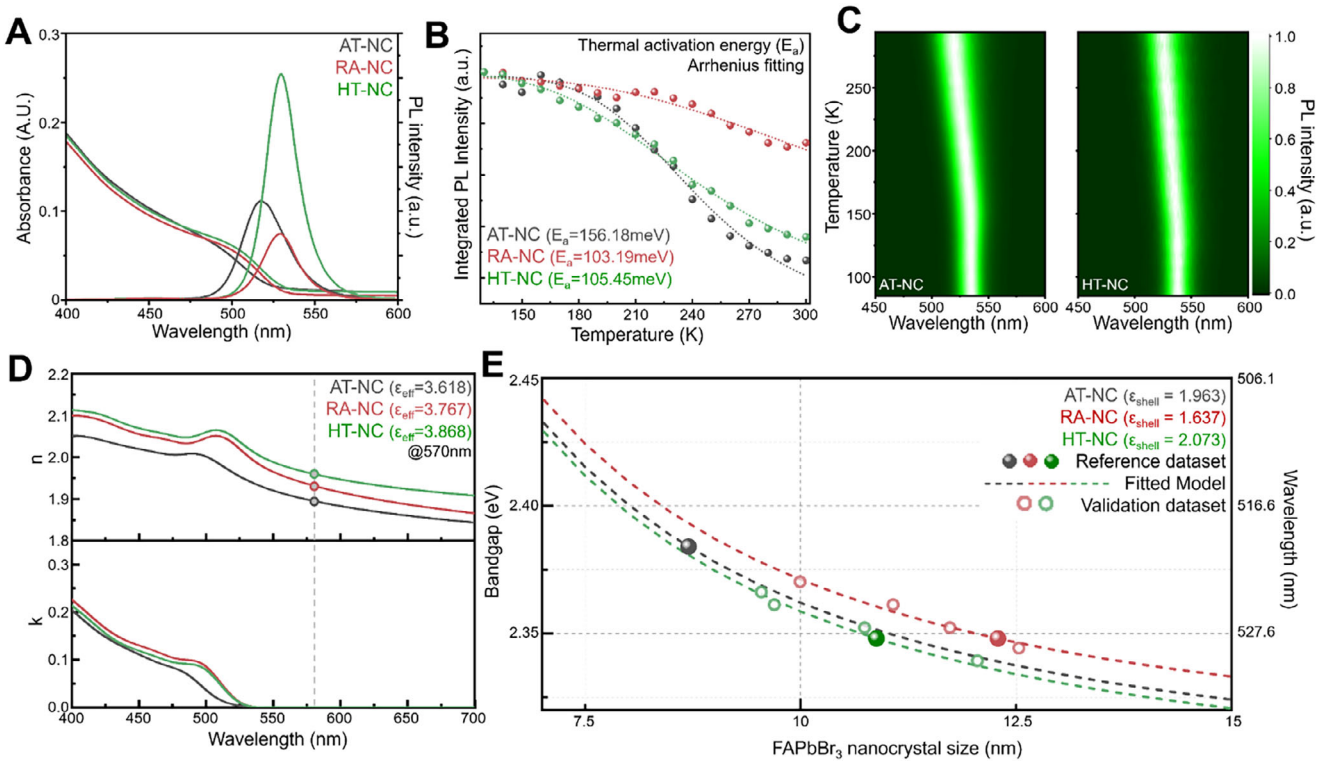

FIGURE 3 | Optical and dielectric characterization of perovskite nanocrystal films. (A) Steady-state PL and UV–vis absorption spectra of AT-NC, RA-NC, and HT-NC films. (B) Temperature-dependent PL data and Arrhenius fitting used to extract thermal activation energies. (C) 3D PL spectra of AT-NC and HT-NC films showing wavelength variations with temperature. (D) Refractive index and extinction coefficient values of the films obtained from spectroscopic ellipsometry. (E) Shell dielectric constants of the films calculated using effective medium approximation of Bruggeman model with estimated bandgap variations as a function of nanocrystal size.

observed spectral behavior. Taken together with the PL results, these findings provide clear experimental evidence that quantum confinement is not the sole confinement mechanism governing the optical transition energy in these perovskite nanocrystal films. Based on the additional incorporation of phosphonic acid in the HT-NCs observed in Figure 2E–H, we suggest that the resulting modification with the compact ligand shell reduces dielectric confinement effect, which influences the emission energy.

To elucidate the contribution of the enhanced dielectric confinement term in the HT-NC films, we measured the effective dielectric constant (ε_{eff}) of the nanocrystal films using ellipsometry (Figure 3D). Each film was characterized via variable-angle spectroscopic ellipsometry (VASE) to determine both its thickness and refractive index, from which the effective dielectric constant was subsequently extracted (Figure S10). At wavelengths above 570 nm, where absorption is negligible, the effective dielectric constant can be approximated as the square of the refractive index. Because the perovskite core has a higher dielectric constant than the organic ligand shell, films with larger cores are expected to exhibit higher effective dielectric constants. Consistent with this trend, the AT-NCs showed the lowest value, while the HT-NCs displayed a clear increase compared with the RA-NCs. At 570 nm, the reference wavelength used for the shell dielectric constant calculation, the effective dielectric constants were 3.618 for the AT-NCs, 3.767 for the RA-NCs, and 3.868 for the HT-NCs.

To extract the shell dielectric constant (ε_{shell}) from the ε_{eff}, we employed the Bruggeman effective medium approximation (EMA) model, which is widely used for dielectric modeling of nanocrystals [30, 31]. In this model, the composite is regarded as a mixture of two components, the nanocrystal core and the surrounding shell, that are assumed to be symmetrically embedded and randomly distributed, with both phases contributing equally to the overall dielectric response. The dielectric constant of single crystal $FAPbBr_3$ was used as the core dielectric constant, and the shell thickness was defined using the ligand length estimated from molecular illustration (Figure S11). The calculated results from each EMA model are summarized in Table S1. In the EMA models, the ε_{shell} of RA-NCs largely decreased to 1.637, while that of HT-NCs slightly increased to 2.073 compared to 1.963 for AT-NCs (Figure 3E). This trend directly reflects the surface reconstruction process, where THF-induced partial detachment of bulky PEA ligands leads to a disordered shell in RA-NCs, whereas subsequent incorporation of phosphonic acid ligands forms a compact and strongly bound shell in HT-NCs. Importantly, an increase in ε_{shell} enhances dielectric screening at the nanocrystal surface, thereby reducing the dielectric mismatch between the core and the shell environment. This reduction in dielectric confinement suppresses the surface-polarization energy which represents induced self-energy of a charge arising from its image charges, leading to a downward renormalization of the band edges [22, 32]. As a result, the optical bandgap energy can be reduced even when the exciton binding energy

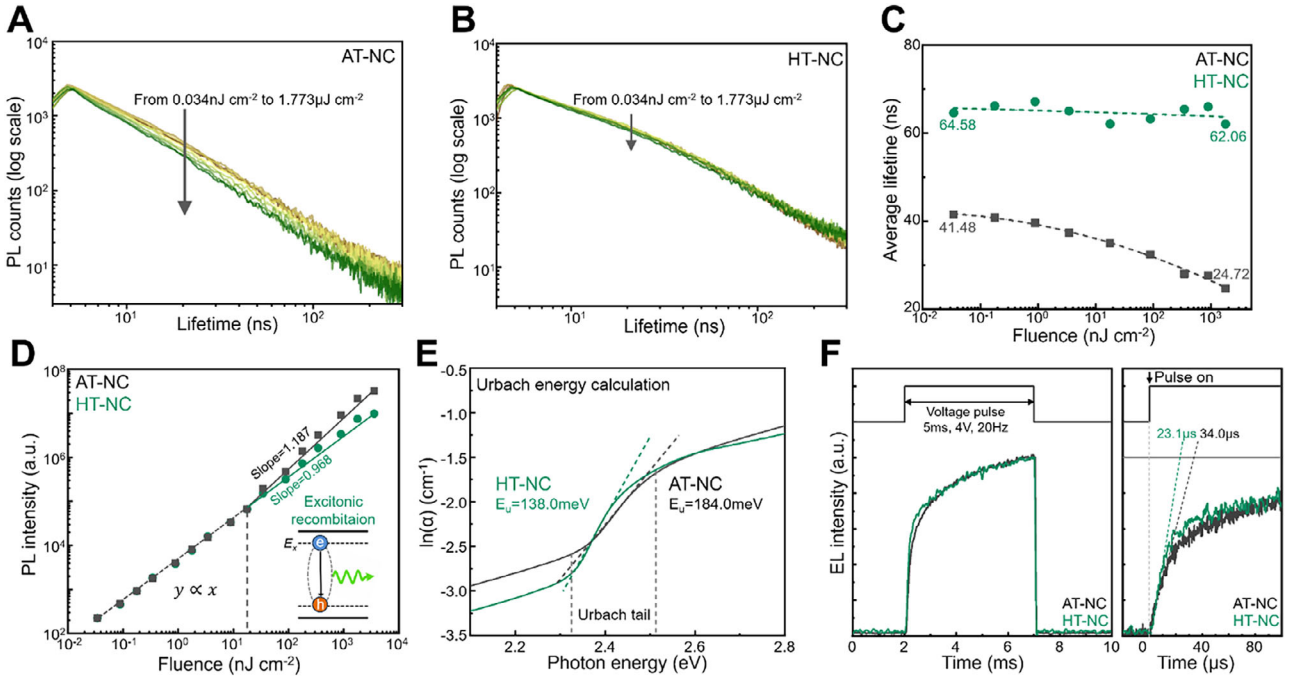

FIGURE 4 | Carrier recombination dynamics and defect characteristics of perovskite nanocrystal films and devices. (A–C) Fluence dependent transient PL decay curves and average PL lifetimes of AT-NC and HT-NC films under excitation fluences ranging from 0.034 nJ cm^{-2} to 1.773 μJ cm^{-2}. (D) Fluence-dependent PL intensity of the films, analyzed as slope vs. fluence, measured over a fluence range of 0.034 nJ cm^{-2} to 3.544 μJ cm^{-2}. (E) Urbach energy (E_u) values extracted from UV–vis absorption spectra of AT-NC and HT-NC films. (F) Transient electroluminescence measurements of AT-NC and HT-NC devices showing EL rise times, performed using 5 ms pulses at 20 Hz and 4 V.

is weakened. These findings provide a clear explanation for why the HT-NCs exhibit an additional redshift compared with the RA-NCs, despite their similar exciton binding energies and smaller crystallite size. Notably, although the RA-NCs possess larger crystallites than the HT-NCs, their lower ε_{shell} results in stronger dielectric confinement, preserving a higher polarization self-energy contribution. In contrast, the HT-NCs experience a more pronounced reduction in dielectric confinement due to the compact phosphonic acid derived shell, which leads to further band-edge renormalization beyond size-dependent quantum confinement [22, 32].

Based on the fact that the three nanocrystal films share the same ε_{core} while differing in both core size and ε_{shell}, we fitted the variation in bandgap using an empirical model that considers the dual confinement effect. The fitting results clearly indicate that a higher ε_{shell} leads to a smaller bandgap even for nanocrystals with the same core size. To validate the consistency of this empirical model, additional samples were prepared by precisely varying the post-treatment reaction time from 2 to 8 s. The nanocrystal size and corresponding optical bandgap were determined using the Scherrer equation based on θ-2θ x-ray diffraction (XRD) measurements and PL spectroscopy, respectively (Figures S12 and S13). As the reaction time increased, gradual particle growth was observed, accompanied by a redshift in the emission wavelength. This trend demonstrates that the dual-confinement modulation approach serves as a finely tunable tool for wavelength control. The additional validation dataset closely followed the fitted model, confirming the reliability of the proposed relationship.

2.4 | Defect and Recombination Dynamics

Then, we investigated the effect of exciton confinement and surface termination on carrier recombination dynamics and defect characteristics, by comparing the AT-NC and HT-NC films as representative systems. We gradually increased the excitation fluence from 0.034 nJ cm^{-2} to 1.773 μJ cm^{-2} and measured the corresponding PL decay dynamics of the in situ nanocrystal films (Figure 4A–C). For the AT-NC film, the average PL lifetime decreased from 41.48 to 24.72 ns with increasing fluence, whereas the HT-NC film exhibited negligible changes in lifetime across the same excitation range. The strong fluence dependence in the AT-NC film indicates the coexistence of abundant traps and strong exciton confinement, which introduce fast nonradiative pathways at low fluence and activate multi-exciton recombination processes at high fluence [33]. In contrast, the negligible lifetime variation in the HT-NC film is consistent with effective trap passivation and reduced exciton binding, leading to more stable recombination dynamics. To further probe the recombination pathways, we examined the fluence dependent PL intensity (Figure 4D). The AT-NC film exhibited nearly linear behavior with a slope close to unity at low fluence, characteristic of excitonic emission, but the slope exceeded unity at high fluence, indicating a transition toward bimolecular recombination as trap states became filled and carrier density increased [33]. In comparison, the HT-NC film maintained a slope close to one for the entire fluence range, highlighting linear excitonic recombination with minimal contributions from trap-related or multi-exciton channels [18]. Analysis of the Urbach energy (E_u) derived from UV–vis spectra further confirmed the impact of

surface termination on defect states (Figure 4E). The HT-NC film showed a lower E_u of 138.0 meV compared to 184.0 meV for AT-NC, consistent with reduced sub-bandgap states and effective suppression of surface traps [34]. The lower energetic disorder facilitates radiative recombination, aligning with the extended PL lifetimes and reduced nonradiative losses. To connect these film-level insights to device operation, we carried out transient electroluminescence measurements. (Figure 4F) The HT-NC device exhibited a faster EL rise time (23.1 μs) than AT-NC (34.0 μs), reflecting the lower trap density and the faster buildup of radiative recombination [35].

2.5 | Device Performance Evaluation

Building on the film-level analysis, the optimized perovskite layers were integrated into PeLEDs as emitters to evaluate their influence on device performance. The device architecture was ITO/BufHIL (40 nm)/AT-NC or HT-NC (40 nm)/TPBi (40 nm)/LiF (1.2 nm)/Al (100 nm) (Figure 5A). The energy levels of the AT-NC and HT-NC films were determined from ultraviolet photoelectron spectroscopy measurements, where the work function and valence band maximum were extracted, and the conduction band minimum was calculated using the optical bandgap (Figure S14). The HT-NC devices exhibited significantly higher efficiencies compared with AT-NCs: A CE_{max} of 99.43 cd A^{-1} and EQE_{max} of 23.51% were achieved, in contrast to 38.42 cd A^{-1} and 8.21% for AT-NCs (Figure 5B–D). Device-to-device reproducibility was confirmed: 38 HT-NC devices fabricated in a single batch exhibited an average EQE of 20.28%, with a relative standard deviation of 8.06% in the EQE values. (Figure 5D). Notably, devices based on HT-NCs exhibited a 42.9% increase in operational lifetime compared to AT-NC-based devices, reflecting improved operational stability enabled by effective surface passivation (Figure S15). In terms of color quality, the HT-NC devices showed stable emission coordinates at (0.177, 0.769) in the CIE 1931 space, with a minimal color shift of 0.001 across the voltage range (Figure 5E,F). The color gamut coverage reached 95.78% of the Rec.2020 green primary, 110.37% of NTSC, and 118.54% of DCI-P3 (Figure 5G). Among state-of-the-art single organic-cation green PeLEDs with EQE exceeding 20%, our device represents the highest reported color gamut coverage value to the best of our knowledge (Figure 5H; Table S2). Furthermore, the chromaticity remained effectively invariant with respect to both driving voltage and viewing angle. Across the operating voltage range, $\Delta u'v'$ values stayed below 0.0014, and across viewing angles from 0°–80°, they remained within 0.0027. These values are significantly lower than the allowable tolerances defined in ANSI/HFES 100 for advanced displays ($\Delta u'v' \leq 0.02$) and the AAPM TG18 recommendations for medical imaging systems ($\leq$0.01), and are even smaller than those reported for state-of-the-art AR/VR headsets such as HoloLens 2 of 0.007 (Figure 5I,J). This result confirms the superior color stability enabled by the hybrid-terminated nanocrystal design [8, 9, 36].

3 | Conclusion

In conclusion, we have demonstrated a dual confinement modulation strategy that enables precise spectral tuning of perovskite nanocrystals into the near-standard-green regime. Through post-synthetic surface reconstruction combined with phosphonic acid coordination, both quantum confinement and dielectric confinement were simultaneously regulated. The enlarged nanocrystal size and compact ligand shell reduced exciton binding energy, suppressed trap states, and improved structural stability. The resulting hybrid-terminated nanocrystals exhibited strong and stable green emission with extended carrier lifetimes and reduced energetic disorder.

Using an EMA model, we deduced that the hybrid shell possessed an increased dielectric constant, and by controlling the reaction time, the emission wavelength could be precisely tuned to near-standard-green regime. When incorporated into PeLEDs, it delivered high efficiencies exceeding 23.5% EQE and achieved 95.78% Rec.2020 coverage, which is the highest values reported among efficient single organic-cation PeLEDs. They also exhibited excellent reproducibility and highly stable chromaticity, maintaining $\Delta u'v'$ values below 0.0014 across the operating voltage range and within 0.0027 over viewing angles up to 80°, both of which are well below commonly accepted tolerances. This work establishes dual confinement modulation as a composition-invariant and intrinsically driven approach to engineer perovskite nanocrystals. The demonstrated combination of spectral precision and chromaticity stability underscores the potential of this strategy for advanced display technologies where color accuracy and stability are critically demanded.

4 | Experimental Section/Methods

4.1 | Materials

Formamidinium bromide (FABr, >99.99%), phenethylammonium bromide (PEABr, >98.0%)were purchased from Greatcell solar., Benzylphosphonic acid (BPA, >97%) was purchased from Acros Organics. N,N-Dimethylformamide (DMF, anhydrous 99.8%) and chlorobenzene (CB, anhydrous 99.8%) were purchased from Sigma-Aldrich. Lead bromide ($PbBr_2$, >98.0%) was purchased from TCI. 2,2′,2′′-(1,3,5-Benzinetriyl)-tris(1-phenyl-1*H*-benzimidazole) (TPBi) was purchased from OSM. Lithium fluoride (LiF) was supplied by Foosung. Unless otherwise stated, all materials were used without purification.

4.2 | Preparation of Precursor Solution

The precursor solution was prepared by dissolving stoichiometric ratios of FABr, $PbBr_2$, and PEABr (molar ratio FABr: $PbBr_2$: PEABr = 1: 1: 0.35) in the corresponding solvent at a concentration of 0.2 M. The antisolvent solution was prepared by dissolving TPBi in chlorobenzene at a concentration of 0.1 wt%. The post-treatment solution was prepared by dissolving BPA in THF at 1 g L^{-1}. Both solutions were thoroughly mixed before use.

4.3 | Fabrication of PeLEDs

Prepatterned indium tin oxide (ITO) (70 nm, 25 mm × 25 mm) glasses were sequentially sonicated in acetone, and 2-propanol for 15 min, and then boiled in 2-propanol for 30 min. The surface of

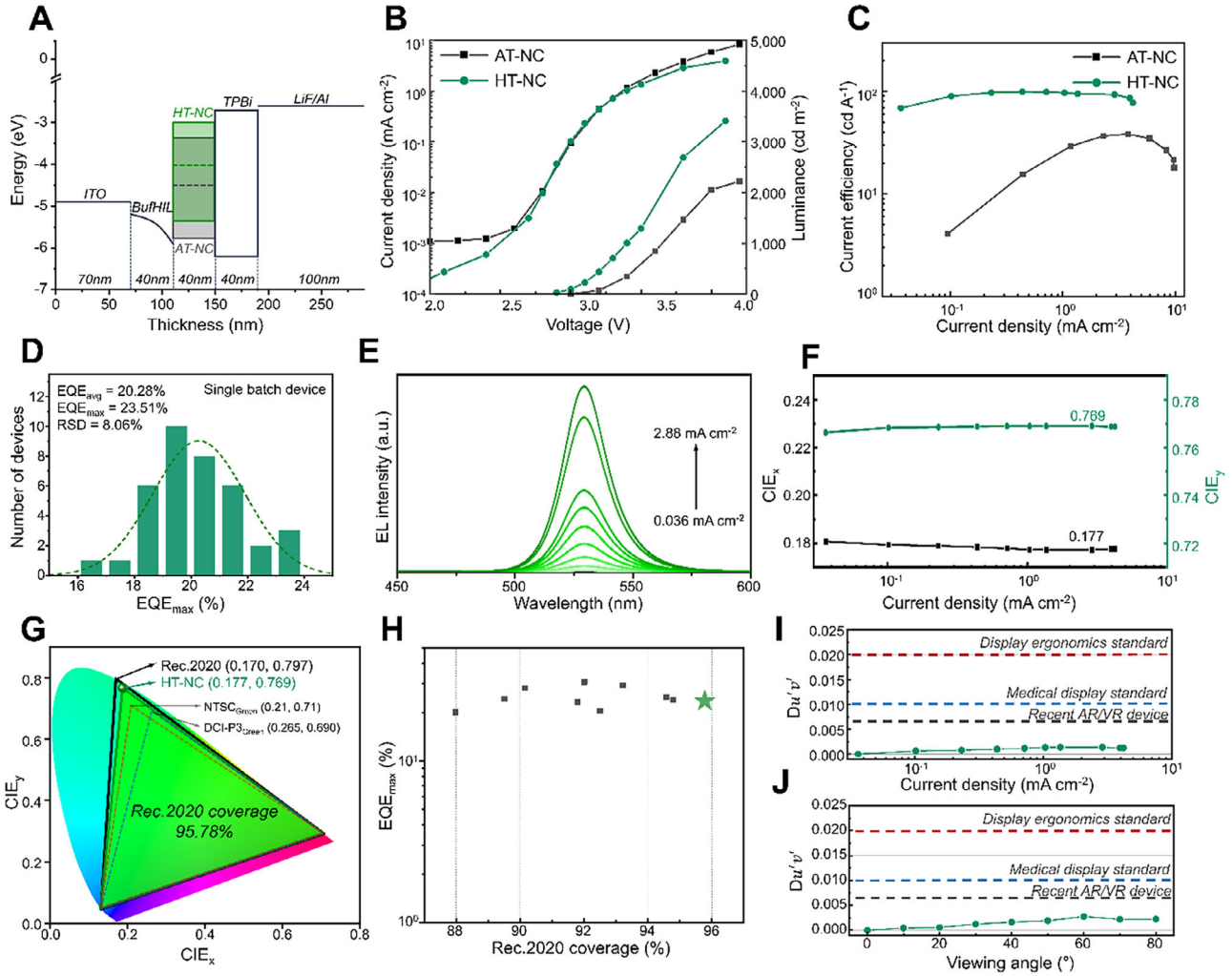

FIGURE 5 | Device performance and chromaticity stability of PeLEDs with surface reconstruction. (A) Schematic architecture of PeLED structure. (B) Current density-voltage-luminance (*J*–*V*–*L*) characteristics. (C) and current efficiency vs. current density of PeLEDs fabricated with AT-NC and HT-NC films. (D) EQE histogram characteristics over 38 HT-NC devices fabricated in single batch. (E,F) EL spectra and corresponding CIE 1931 color coordinates of HT-NC devices under varying voltages. (G) Color gamut coverages of HT-NC devices with respect to Rec.2020, NTSC, and DCI-P3 standards. (H) Summarized EQE-Rec.2020 coverage of recently published state-of-the-art single organic-cation green PeLEDs. (I,J) Voltage- and angle-dependent chromaticity stability of HT-NC devices, evaluated using $\Delta u'v'$ values and compared with ANSI/HFES 100, AAPM TG18, and reported AR/VR device metrics.

ITO substrates underwent ultraviolet-ozone treatment to achieve a hydrophilic surface. We used a previously described method to prepare a buffer hole-injection layer (BufHIL) that had a gradient work function, by inducing vertical self-organization of PEDOT:PSS (CLEVIOS P VP AI4083) and PFI copolymer to have surface-enriched PFI layer; the solution with 1:1 weight ratio of PEDOT:PSS to PFI was spin coated to form a 35 nm thickness, then annealed at 150 °C for 15 min. After baking, the substrates were transferred to a vacuum chamber (<10^{-7} Torr), where a LiF monolayer of approximately 4 nm was deposited at a rate of 1 Å s^{-1} to enhance surface wettability. The substrates were then moved into an N_2-filled glovebox for deposition of the perovskite film. $FAPbBr_3$ in situ nanocrystal films were deposited by spin coating at 4000 rpm for 30s. In the spin-coating step, the antisolvent solution was dripped 6 s from the start. After spin coating, the films were left to rest for 10 s, followed by the application of the post-treatment solution and a reaction time of 6 s. Subsequently, the films were spin-coated again at 4000 rpm for 30 s to remove the residual solvent completely. Samples were then moved to the vacuum chamber (<10^{-7} Torr) to sequentially deposit TPBi (40 nm), LiF (1.2 nm) and Al (100 nm). The active area of 4.3 mm^2 was defined by shadow masking during deposition of the cathode. Finally, the fabricated PeLEDs were encapsulated in a glovebox under a controlled N_2 atmosphere (O_2 < 2.0 ppm, H_2O < 1.0 ppm) by using a glass lid and UV-curable epoxy resin with 20 min of UV (365 nm) treatment.

4.4 | Perovskite Film Characterization

Steady-state photoluminescence (PL) spectra of perovskite film and ultraviolet–visible (UV–vis) absorption spectra of perovskite film and precursor solution were measured using a JASCO FP8500 spectrofluorometer and V-770 UV–vis spectrophotometer.

GIWAXS was performed on the films at beamlines 3C of the Pohang Accelerator Laboratory (PAL), Republic of Korea. The incident angle of the x-ray beam (λ = 1.0973 Å) on a sample was fixed at 0.1°.

For transient PL decay measurements, a FluoTime 300 spectrometer was used. A picosecond-pulse laser head (LDH-P-C-405B, PicoQuant) was used to excite the samples at a laser wavelength of 405 nm. A photon-counting detector (PMA Hybrid 07) and time-correlated single-photon-counting module (PicoHarp, PicoQuant) were used to detect the PL decay and calculate the PL lifetimes of samples. The average PL decay lifetimes of perovskite films were obtained by fitting transient PL curves using a tri-exponential decay function. For the temperature-dependent PL measurements, the sample was mounted in a cryostat (Advanced Research Systems) under vacuum, and the emission spectrum was analyzed using a 405 nm laser diode (PicoQuant) at a low fluence with in excitonic recombination regime. E_a was calculated using the Arrhenius equation, $I_T = I_0/(1 + A\exp(-E_a/kT))$, where I_T was the integrated PL intensity, I_0 was PL intensity at 0 K, A was constant, k was Boltzmann constant, and T was temperature.

For power-dependent PL measurements, an emission attenuator was adjusted to maintain the pile-up rate below 1% and thereby minimize instrumental errors associated with increasing signal intensity at higher fluence. To prevent sample degradation during measurement, the fluence was increased stepwise from low to high. The excitation power of the laser diode was monitored using a power meter (Thorlabs, PM120D).

For TEM characterization, the perovskite films were prepared on 15 nm thick silicon nitride (Si_3N_4) grids that had been pre-treated to be hydrophilic. To replicate the exact growth conditions of the films, a 5 nm layer of LiF was deposited onto the grids prior to the sample preparation. The prepared grids underwent the same thermal annealing process as the actual thin films and were subsequently stored in a vacuum overnight to ensure the complete removal of residual solvents. TEM analysis was performed using a JEOL JEM-2100PLUS microscope at an accelerating voltage of 200 kV. The average particle size was estimated by measuring the area of individual nanocrystals and calculating the equivalent diameter assuming a circular geometry.

Solid-state Fourier-transform infrared (FT-IR) spectra were acquired to investigate the chemical bonding and ligand environments of the perovskite films. To obtain a sufficient signal-to-noise ratio from the thin-film samples, the perovskite layers were coated on glass substrates and then carefully collected in solid form using a razor blade. The measurements were conducted in attenuated total reflectance (ATR) mode using a Nicolet iS50 spectrometer (Thermo Fisher Scientific). To minimize atmospheric degradation, the samples were vacuum-packaged and transported immediately before the measurements.

XPS and UPS spectra were measured using a photoelectron spectrometer (Versaprobe III, Ulvac-phi), a monochromatic AlK_α line (1486.6 eV) was used for XPS and He I line (21.22 eV) for UPS. To minimize damage from air exposure, the samples were transferred directly from the glovebox to the XPS antechamber using a vacuum holder.

Images of the surfaces were obtained using a field-emission scanning electron microscope (SEM) (SUPRA 55VP) operated at 2 kV. For high-resolution measurements, the samples were coated with a 5 nm Pt layer deposited at a rate of 1 Å s^{-1}.

Variable angle spectroscopic ellipsometer (J.A. Woollam Co.) was used for measuring the refractive index and thickness of the layers. Ellipsometric data was acquired in the range of the wavelength from 200 to 1650 nm and the detection angle from 45° to 75° with 5° intervals.

The theoretical calculations were performed using the VASP package based on the density functional theory (DFT). The Perdew-Burke-Ernzerhof (PBE) functional with Grimme's D3 dispersion correction was employed. The vacuum region of 20 Å was used to avoid the periodic interaction. For the relaxation of geometric structures, the kinetic energy cutoff was set to 450 eV. A Γ-centered k-point mesh of 3 × 3 × 3 was used.The stress force and energy convergence criteria were chosen as 0.01 eV/Å and 10–5 eV, respectively.

To describe the size- and environment-dependent bandgap shift in perovskite nanocrystals, a simplified empirical model was developed by considering both quantum and dielectric confinement effects. In general, the bandgap of a nanocrystal increases with decreasing particle size due to carrier quantization (quantum confinement), and was further affected by the dielectric mismatch between the perovskite core and its surrounding medium (dielectric confinement). The quantum term was typically proportional to d^{-2}, reflecting the kinetic energy increase of spatially confined carriers, whereas the dielectric term originates from the modified Coulomb interaction, which scales weakly with size ($\propto 1/d$) and depends on the ratio $\varepsilon_{core}/\varepsilon_{shell}$. For practical fitting of experimental data, these two contributions were separated and expressed in a compact form as Equation 1. where A, B and C were empirical parameters that incorporate material-specific constants such as the dielectric mismatch. This form enabled simultaneous consideration of both quantum and dielectric confinement effects while maintaining mathematical simplicity suitable for fitting experimental observations.

$$E_g\ (d) = E_g^{bulk} + A*d^{-2} + B*\varepsilon_{shell}^{-1} + C*\varepsilon_{shell}^{-2} \quad (1)$$

4.5 | PeLEDs Device Characterization

The current density-voltage-luminescence (J-V-L) characteristics of PeLEDs were measured using a spectroradiometer (CS-2000, Minolta) and an electrical source-measurement unit (Keithley 236). Full angular electroluminescence distribution was measured by rotating observable angles to spectroradiometer, and then exact EQE was calculated based-on Lambertian angle factor. Transient EL signals were recorded using a photomultiplier tube detector (PDS-1, Dongwoo Optron Co.) connected to an oscilloscope (Infiniium 54832D, Agilent), while electrical pulses were applied using a function generator (AFG2021, Tektronix).

By using electrochemical impedance spectroscopy workstation (SP-200 potentiostat, Biologic), capacitance-voltage measurement was conducted to evaluate charge balance in the LED devices.

Operational lifetime of PeLEDs was measured under constant-current conditions by simultaneously tracking brightness and applied voltage using an M760 Lifetime Analyzer (McScience) with a control computer.

To quantify the color stability, the chromaticity deviation ($\Delta u'v'$) was calculated using the CIE 1976 UCS color space. The (u', v') coordinates were derived from the CIE 1931 (x, y) coordinates.

$$u' = 4x \,/\, (-2x + 12y + 3)\; v' = 9y \,/\, (-2x + 12y + 3) \quad (2)$$

The $\Delta u'v'$ value, representing the perceptual color difference, was calculated using the following equation:

$$\Delta u'v' = \left[(u'_i - u'_0)^2 + (v'_i - v'_0)^2 \right]^{1/2} \quad (3)$$

where (u'_0, v'_0) was the reference chromaticity coordinate at the initial state (initial voltage or 0° viewing angle) and (u'_i, v'_i) was the coordinate at a specific measurement point.

Author Contributions

E.Y. and T.-W.L. initiated and designed the study. E.Y. and K-H.L. conducted the experiments. E.Y., K.-H.L., C.-Y.P., M.-J.S., Y.S., K.Y.J., J.P., J.S.K. and E.K. contributed to the analysis and interpretation of the results. T.-W.L. supervised the work. E.Y. drafted the first version of the manuscript, with assistance from T.-W.L.

Acknowledgements

This work was supported by the National Research Foundation of Korea (NRF) grant funded by the Korean government (Ministry of Science, ICT & Future Planning) (RS202500560490 and 2022M3H4A1A04096380).

Conflicts of Interest

The authors declare no conflict of interest.

Data Availability Statement

The data that support the findings of this study are available from the corresponding author upon reasonable request.

References

1. T.-H. Han, K. Y. Jang, Y. Dong, R. H. Friend, E. H. Sargent, and T.-W. Lee, "A Roadmap for the Commercialization of Perovskite Light Emitters," *Nature Reviews Materials* 7, no. 10 (2022): 757–777, https://doi.org/10.1038/s41578-022-00459-4.

2. Z.-K. Tan, R. S. Moghaddam, M. L. Lai, et al., "Bright Light-emitting Diodes Based on Organometal Halide Perovskite," *Nature Nanotechnology* 9, no. 9 (2014): 687–692, https://doi.org/10.1038/nnano.2014.149.

3. Y. Kim, H. Cho, J. H. Heo, et al., "Multicolored Organic/Inorganic Hybrid Perovskite Light-Emitting Diodes," *Advanced Materials* 27, no. 7 (2014): 1248–1254, https://doi.org/10.1002/adma.201403751.

4. H. Cho, S.-H. Jeong, M.-H. Park, et al., "Overcoming the Electroluminescence Efficiency Limitations of Perovskite Light-emitting Diodes," *Science* 350, no. 6265 (2015): 1222–1225, https://doi.org/10.1126/science.aad1818.

5. J. S. Kim, J.-M. Heo, G.-S. Park, et al., "Ultra-bright, Efficient and Stable Perovskite Light-emitting Diodes," *Nature* 611, no. 7937 (2022): 688–694, https://doi.org/10.1038/s41586-022-05304-w.

6. C. Peng, H. Yao, O. Ali, et al., "Weakly Space-confined All-inorganic Perovskites for Light-emitting Diodes," *Nature* 643, no. 8070 (2025): 96–103, https://doi.org/10.1038/s41586-025-09137-1.

7. W. Bai, T. Xuan, H. Zhao, et al., "Perovskite Light-Emitting Diodes with an External Quantum Efficiency Exceeding 30%," *Advanced Materials* 35, no. 39 (2023), https://doi.org/10.1002/adma.202302283.

8. Human Factors and Ergonomics Society (HFES), *ANSI/HFES 100–2007: Human Factors Engineering of Computer Workstations*, 2007.

9. E. Samei, A. Badano, D. Chakraborty, et al., "Assessment of Display Performance for Medical Imaging Systems: Executive Summary of AAPM TG18 Report," *Medical Physics* 32, no. 4 (2005): 1205–1225, https://doi.org/10.1118/1.1861159.

10. Q. A. Akkerman, V. D'Innocenzo, S. Accornero, et al., "Tuning the Optical Properties of Cesium Lead Halide Perovskite Nanocrystals by Anion Exchange Reactions," *Journal of the American Chemical Society* 137, no. 32 (2015): 10276–10281, https://doi.org/10.1021/jacs.5b05602.

11. M. C. Brennan, S. Draguta, P. V. Kamat, and M. Kuno, "Light-Induced Anion Phase Segregation in Mixed Halide Perovskites," *ACS Energy Letters* 3, no. 1 (2017): 204–213, https://doi.org/10.1021/acsenergylett.7b01151.

12. S. Xing, Y. Yuan, G. Zhang, et al., "Energy-Efficient Perovskite LEDs with Rec. 2020 Compliance," *ACS Energy Letters* 9, no. 8: 3643–3651, https://doi.org/10.1021/acsenergylett.4c01501.

13. M. Jiang, L. Li, Z. Qi, and F. Wang, "Efficient Rec. 2020 Compliant Pure-Green Mixed-Cation Perovskite Light-Emitting Diodes with Multifunctional Co-Additives," *Advanced Materials* 37, no. 29 (2025), https://doi.org/10.1002/adma.202503683.

14. D. Sapori, M. Kepenekian, L. Pedesseau, C. Katan, and J. Even, "Quantum Confinement and Dielectric Profiles of Colloidal Nanoplatelets of Halide Inorganic and Hybrid Organic–inorganic Perovskites," *Nanoscale* 8, no. 12 (2016): 6369–6378, https://doi.org/10.1039/c5nr07175e.

15. X. Hou, J. Kang, H. Qin, et al., "Engineering Auger Recombination in Colloidal Quantum Dots via Dielectric Screening," *Nature Communications* 10, no. 1 (2019), https://doi.org/10.1038/s41467-019-09737-2.

16. S. Caicedo-Dávila, P. Caprioglio, F. Lehmann, et al., "Effects of Quantum and Dielectric Confinement on the Emission of Cs-Pb-Br Composites," *Advanced Functional Materials* 33, no. 46 (2023), https://doi.org/10.1002/adfm.202305240.

17. M. R. Filip, D. Y. Qiu, M. Del Ben, and J. B. Neaton, "Screening of Excitons by Organic Cations in Quasi-Two-Dimensional Organic–Inorganic Lead-Halide Perovskites," *Nano Letters* 22, no. 12 (2022): 4870–4878, https://doi.org/10.1021/acs.nanolett.2c01306.

18. Y. Jiang, M. Cui, S. Li, et al., "Reducing the Impact of Auger Recombination in Quasi-2D Perovskite Light-emitting Diodes," *Nature Communications* 12, no. 1 (2021), https://doi.org/10.1038/s41467-020-20555-9.

19. Z. Xiao, R. A. Kerner, L. Zhao, et al., "Efficient Perovskite Light-emitting Diodes Featuring Nanometre-sized Crystallites," *Nature Photonics* 11, no. 2 (2017): 108–115, https://doi.org/10.1038/nphoton.2016.269.

20. M. Park, J. Park, J. Lee, et al., "Efficient Perovskite Light-Emitting Diodes Using Polycrystalline Core–Shell-Mimicked Nanograins," *Advanced Functional Materials* 29, no. 22 (2019), https://doi.org/10.1002/adfm.201902017.

21. E. Yoon, J. S. Kim, J.-M. Heo, S.-C. Lee, and T.-W. Lee, "Precursor-solvent Coordination Control for Defect Suppression in Perovskite Light-emitting Diodes," *Nano Research Energy* 5, no. 2 (2026): 9120219, https://doi.org/10.26599/nre.2026.9120219.

22. H. M. Jang, J. Park, S. Kim, and T.-W. Lee, "Quantum-confinement Effect on the Linewidth Broadening of Metal Halide Perovskite-based Quantum Dots," *Journal of Physics: Condensed Matter* 33, no. 35 (2021): 355702, https://doi.org/10.1088/1361-648x/ac00db.

23. G. Mannino, I. Deretzis, E. Smecca, et al., "Temperature-Dependent Optical Band Gap in CsPbBr3, MAPbBr3, and FAPbBr3 Single Crystals," *The Journal of Physical Chemistry Letters* 11, no. 7 (2020): 2490–2496, https://doi.org/10.1021/acs.jpclett.0c00295.

24. M. Qin, P. F. Chan, and X. Lu, "A Systematic Review of Metal Halide Perovskite Crystallization and Film Formation Mechanism Unveiled by in Situ GIWAXS," *Advanced Materials* 33, no. 51 (2021), https://doi.org/10.1002/adma.202105290.

25. F. Bertolotti, A. Vivani, F. Ferri, et al., "Size Segregation and Atomic Structural Coherence in Spontaneous Assemblies of Colloidal Cesium Lead Halide Nanocrystals," *Chemistry of Materials* 34, no. 2 (2022): 594–608, https://doi.org/10.1021/acs.chemmater.1c03162.

26. J. De Roo, M. Ibáñez, P. Geiregat, et al., "Highly Dynamic Ligand Binding and Light Absorption Coefficient of Cesium Lead Bromide Perovskite Nanocrystals," *ACS Nano* 10, no. 2 (2016): 2071–2081, https://doi.org/10.1021/acsnano.5b06295.

27. R. L. Penn and J. F. Banfield, "Imperfect Oriented Attachment: Dislocation Generation in Defect-Free Nanocrystals," *Science* 281, no. 5379 (1998): 969–971, https://doi.org/10.1126/science.281.5379.969.

28. E. J. Juarez-Perez, M. Wuβler, F. Fabregat-Santiago, et al., "Role of the Selective Contacts in the Performance of Lead Halide Perovskite Solar Cells," *The Journal of Physical Chemistry Letters* 5, no. 4 (2014): 680–685, https://doi.org/10.1021/jz500059v.

29. M. Baranowski and P. Plochocka, "Excitons in Metal-Halide Perovskites," in *Advanced Energy Materials* (2020), https://doi.org/10.1002/aenm.201903659.

30. D. B. Dement, M. Puri, and V. E. Ferry, "Determining the Complex Refractive Index of Neat CdSe/CdS Quantum Dot Films," *The Journal of Physical Chemistry C* 122, no. 37 (2018): 21557–21568, https://doi.org/10.1021/acs.jpcc.8b04522.

31. S.-H. Park, J. Kim, M. J. Kim, M. W. Kim, R. A. Taylor, and K. Kyhm, "Complex Refractive Index Spectrum of CsPbBr3 Nanocrystals via the Effective Medium Approximation," *Nanomaterials* 15, no. 3 (2025): 181, https://doi.org/10.3390/nano15030181.

32. L. E. Brus, "Electron–electron and Electron-hole Interactions in Small Semiconductor Crystallites: the Size Dependence of the Lowest Excited Electronic state," *The Journal of Chemical Physics* 80, no. 9 (1984): 4403–4409, https://doi.org/10.1063/1.447218.

33. J. M. Richter, M. Abdi-Jalebi, A. Sadhanala, et al., "Enhancing Photoluminescence Yields in Lead Halide Perovskites by Photon Recycling and Light Out-coupling," *Nature Communications* 7, no. 1 (2016), https://doi.org/10.1038/ncomms13941.

34. M. Li, P. Huang, and H. Zhong, "Current Understanding of Band-Edge Properties of Halide Perovskites: Urbach Tail, Rashba Splitting, and Exciton Binding Energy," *The Journal of Physical Chemistry Letters* 14, no. 6 (2023): 1592–1603, https://doi.org/10.1021/acs.jpclett.2c03525.

35. Y. Shen, X.-M. Hu, M.-L. Guo, Y.-Q. Li, and J.-X. Tang, "Unveiling the Carrier Dynamics of Perovskite Light-Emitting Diodes via Transient Electroluminescence," *The Journal of Physical Chemistry Letters* 15, no. 31 (2024): 7916–7923, https://doi.org/10.1021/acs.jpclett.4c01971.

36. S. König, S. Siebers, and C. Backhaus, "Image Quality Assessment of Augmented Reality Glasses as Medical Display Devices (HoloLens 2)," *Applied Sciences* 15, no. 14 (2025): 7648, https://doi.org/10.3390/app15147648.

Supporting Information

Additional supporting information can be found online in the Supporting Information section.

Supporting File: adfm74846-sup-0001-SuppMat.docx.